

Contents

Introduction	3
Bicycle Model and Handling analysis	5
Bicycle model	5
Model development.....	5
Twin-track model	10
Model development.....	10
Results	11
Suspension Dynamics and Ride Optimisation	13
Single-Degree of Freedom	13
Optimization	14
Two-Degree of Freedom.....	15
Optimization	15
Four-Degree of Freedom.....	17
Results	17
Optimization	18
Individual reflection	20
Bibliography	21
Appendix	23

Figures

Figure 1. Schematic of bicycle model.....	3
Figure 2. 4-Degrees of Freedom half vehicle model	3
Figure 3. Understeering ADAMS vehicle model	5
Figure 4. Non-linear cornering stiffness spline.....	6
Figure 5. Understeer gradient for the vehicle model.....	7
Figure 6. Cornering equation for linear and non-linear bicycle model	7
Figure 7. Bicycle model US slip angles	7
Figure 8. Bicycle model US lateral forces	7
Figure 9. Bicycle model NS slip angles	8
Figure 10. Bicycle model NS lateral forces	8
Figure 11. Bicycle model OS slip angles	8
Figure 12. Bicycle OS lateral forces.....	8
Figure 13. Bicycle models yaw rates	8
Figure 14. Bicycle models position along X,Y	9
Figure 15. Twin-track model	10
Figure 16. Twin-track X,Y position	11

Figure 17. Twin-track US Slip angles.....	11
Figure 18. Twin-track US Lateral force.....	11
Figure 19. Twin-track NS Slip angles	11
Figure 20. Twin-track NS Lateral force.....	11
Figure 21. Twin-track OS Slip angles	11
Figure 22. Twin-track OS Lateral forces	11
Figure 23. Twin-track model Yaw rates	12
Figure 24. SDoF model	13
Figure 25. Damping spline	13
Figure 26. Road input spline	13
Figure 27. Spring force RMS damping coefficient optimization study	14
Figure 28. Comparison of vertical body acceleration for the SDoF model	14
Figure 29. Comparison of tyre contact patch for the SDoF model	14
Figure 30. TDoF model.....	15
Figure 31. RMS Design studies for damping coefficient	15
Figure 32. TDoF Component frequency study	16
Figure 33. TDoF modes of vibration	16
Figure 34. Comparison of TDoF model vertical body acceleration	16
Figure 35. Comparison of TDoF model tyre force variation	16
Figure 36. FDoF model	17
Figure 37. Original CoG location hub displacements	17
Figure 38. Rear hub displacement analysis	18
Figure 39. Comparison of vertical body acceleration for the FDoF model	18
Figure 40. Comparison of body pitch for the FDoF model.....	19
Figure 41. Comparison of front tyre force for the FDoF model	19
Figure 42. Comparison of rear tyre force for the FDoF model.....	19

Tables

Table 1. Optimization values for FDoF model	18
Table 2. Input metrics for bicycle model.....	23
Table 3. Input metrics for twin-track model	23
Table 4. Input metrics for SDoF model	23
Table 5. Optimization values for SDoF model	23
Table 6. Input metrics for TDoF model.....	24
Table 7. Optimization values for TDoF model.....	24
Table 8. Input metrics for FDoF model	24
Table 9. Optimization values for FDoF model	24

Introduction

The study of vehicle dynamics is essential to understanding and optimizing the vehicle's performance, allowing for improved handling, stability and ride quality under high-speed conditions.

Bicycle models are important for characterising and optimizing the vehicle's lateral handling, monitoring aspects like yaw stability, sideslip or vehicle trajectory. For the most accurate vehicle representation, it is best to use a non-linear bicycle model, as in conditions which include a high lateral load, vehicle performance representation usually falls short due to the non-linear nature of vehicle dynamics (Ren, H. et al., 2014).

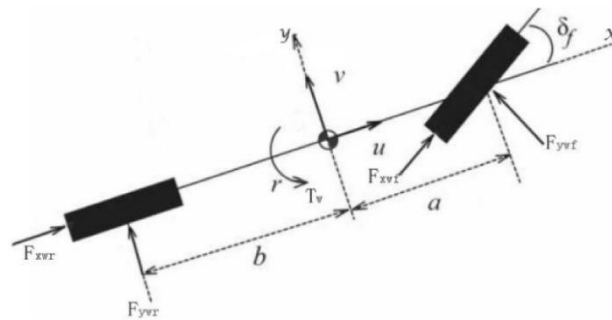


Figure 1. Schematic of bicycle model

To gain a deeper understanding of the lateral force vehicle dynamics, a twin-track model can be used, in order to account for the vertical load change between wheels on the same track, thus allowing the understanding of the load transfer effects on the vehicle dynamics.

On the other hand, understanding the tyre and suspension dynamics and its interaction with the road it's a key factor in improving the vehicle's vertical handling and ride quality, by means of minimizing the dynamic tyre load variations, reducing response times and maintaining consistent performance (Oraby, W. A. H. et al., 2007).

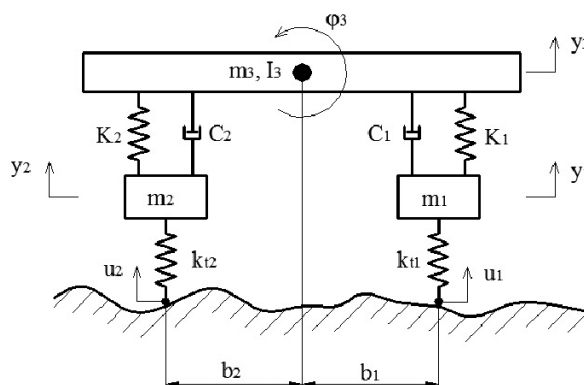


Figure 2. 4-Degrees of Freedom half vehicle model

The use of these models is of great importance for motorsport, as they allow maximising cornering speed, power transfer from the engine to the track and driver confidence in the behaviour of the vehicle.

Faculty of Technology, Design & Environment

School of Engineering, Computing & Mathematics

Future applications of these models can be seen already with autonomous driving vehicles, as these models will allow the algorithms to predict the correct behaviour of the vehicle, maximizing comfort and security for road-going vehicles, and on-track performance for motorsports-oriented vehicles (Lee, J. Y. S., 2017).

Bicycle Model and Handling analysis

Bicycle model

Model development

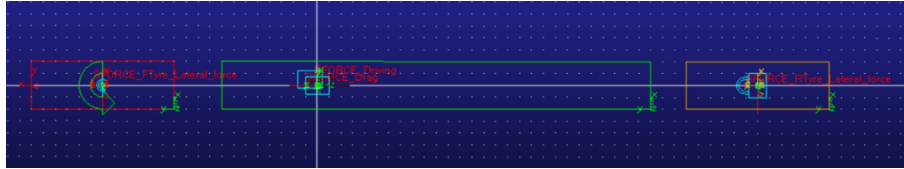


Figure 3. Understeering ADAMS vehicle model

For the vehicle model, a 2022 Honda Civic Type-R has been selected. Input parameters are available in table 2 on the appendix.

The model used is the front wheel steering model, developed making use of three bodies that serve as both wheels and the vehicle body, in a way that the rear wheel rotation is fixed to follow the body rotation, while the front wheel experiments the steering angle applied to the model.

- **Understeering model:** the CoG is placed closer to the front track of the vehicle, achieving 67.1:32.9 distribution. Tyre cornering stiffness is higher at the front due to the weight distribution.
- **Neutral-steering model:** the CoG is placed in the middle of the wheelbase, achieving 50:50 distribution. Tyre cornering stiffness is equal for both tracks due to the weight distribution.
- **Oversteering model:** The furthest distribution possible is 46.5:53.5. Tyre cornering stiffness is higher at the rear due to the weight distribution.

We obtain the vehicle body's moments of inertia, with the assumption of a point mass, since the location of all the vehicle mass is unknown, for a rectangular cuboid:

$$I_{xx_c} = \frac{1}{12}m(H^2 + W^2); I_{yy_c} = \frac{1}{12}m(L^2 + H^2); I_{zz_c} = \frac{1}{12}m(L^2 + W^2)$$

All tyre masses and inertias have been entered with a value of 1, to allow the model to run correctly, with all masses and inertias entered in the vehicle body.

Tyre slip angle is defined as “...*the angle at which the moving tyre is presented to the road when viewed in plan.*” (Blundell, 2004, p. 30). This can be calculated based on the lateral tyre speed related to the actual vehicle traveling speed:

$$\alpha = \arctan\left(\frac{V_y}{V_x}\right)$$

In order to represent the change in lateral force produced by a tyre, the cornering stiffness must also be calculated for the specific tyres of the vehicle.

This can be obtained either through experimental data or by a series of calculations, achieving a less accurate result.

First, the centripetal force (F_c) for a specific radius and speed must be calculated, afterwards, this is multiplied by the weight distribution percentage, in order to obtain the track specific tyre stiffness (Balkwill, 2018):

$$F_c = \frac{m * v^2}{r} ; F_{Yf} = F_c * W_f ; F_{Yr} = F_c * W_r$$
$$C_f = F_{Yf} * \alpha ; C_r = F_{Yr} * \alpha$$

For our model, the tyres cornering stiffnesses have been selected as an approximation to the experimental cornering stiffnesses obtained for a 2020 Volkswagen Golf, as both vehicles share a very similar wheelbase and weight distribution (Balaga, S., 2024):

$$C_f = 1,500N/deg ; C_r = 1,400N/deg$$

This stiffness is later modified depending on the weight distribution along the vehicle's wheelbase to correctly represent the change in lateral dynamics.

To run the simulation, velocity has been set at 30m/s and steering angle has been configured to a step function at -10 degrees, enabling the comparison between linear and non-linear tyre behaviour, avoiding the small angle approximations.

Vehicle drag force and driving force should also be calculated. These will allow us to maintain the experiment at a constant speed of 30m/s (Balkwill, 2018):

$$Drag_{force} = C_d * V^2 ; Driving_{force} = C_d * V_{required}^2$$

The non-linear tyre stiffness coefficient spline used for the model is the following:

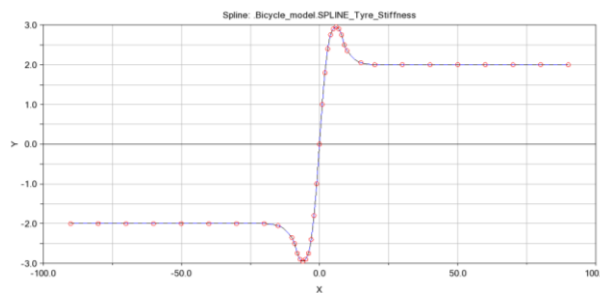


Figure 4. Non-linear cornering stiffness spline

Although this spline allows for slip angles up to 90 degrees, this would not be possible to achieve by a real experiment, as the tyre would separate from the rim bead before reaching those angles, due to the effect of high lateral forces. For passenger vehicles, usual maximum slip angle is 5 degrees (Simpletire, 2022), for motorsports applications, this threshold is augmented to 6 degrees (Suspensionsecrets, n.d.).

First, the understeer gradient (Balkwill, 2018) for the different vehicle configurations is obtained: $K = \frac{m(bC_R - aC_F)}{LC_F C_R}$

Understeer gradient			
	Understeer	Neutral-steer	Oversteer
M (kg)	1430	1430	1430
L (mm)	2735	2735	2735
a (mm)	900	1367.5	1835
b (mm)	1835	1367.5	900
C _f (N/mm)	1500	1450	1400
C _r (N/mm)	1400	1450	1500
K	0.30	0.00	-0.30

Figure 5. Understeer gradient for the vehicle model

Afterwards, we apply the equation of cornering (Balkwill, 2018), to characterize the vehicle's behaviour for both linear and non-linear cornering stiffness during the experiment:

$$\delta = \frac{L}{R} + (\alpha_F - \alpha_R)$$

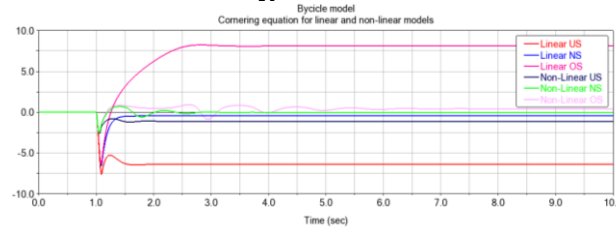


Figure 6. Cornering equation for linear and non-linear bicycle model

Expected values are: $\delta < 0 \rightarrow US$; $\delta = 0 \rightarrow NS$; $\delta > 0 \rightarrow OS$.

These values are achieved in the different experiments, denoting the correct compliance of the model in terms of understeering behaviour.

We can also observe the reduction of the values for the non-linear models, this is due to the correct representation of the slip angles, highlighting the lack of real representation of the linear model beyond the small-angle approximation.

We can observe a more realistic representation of the slip angles for the non-linear model, as a slip angle as high as those achieved by the linear model will include the risk of tyre failure, as it may separate from the rim.

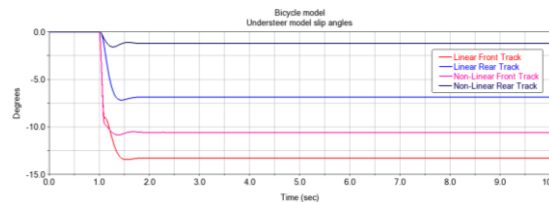


Figure 7. Bicycle model US slip angles

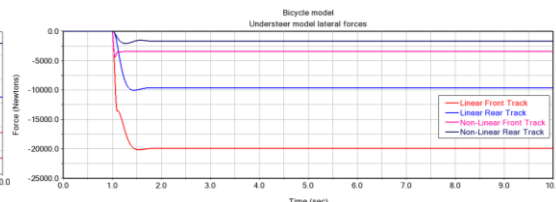


Figure 8. Bicycle model US lateral forces

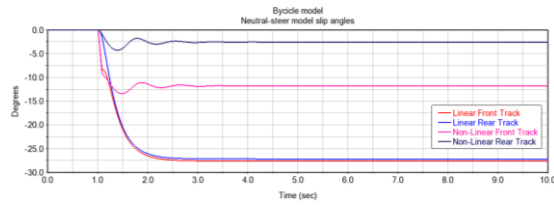


Figure 9. Bicycle model NS slip angles

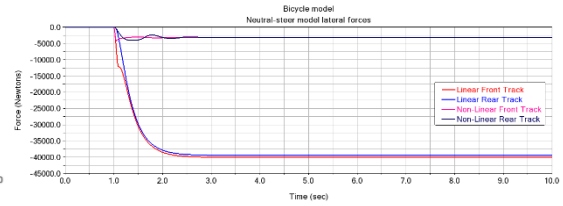


Figure 10. Bicycle model NS lateral forces

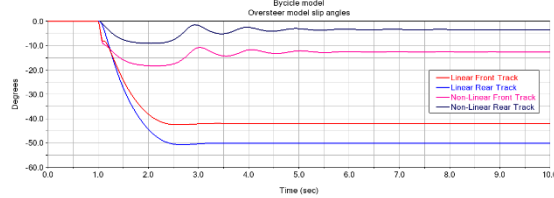


Figure 11. Bicycle model OS slip angles

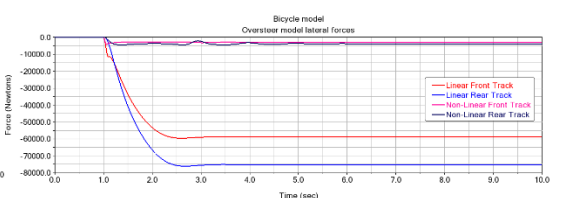


Figure 12. Bicycle OS lateral forces

As for the lateral forces, we can observe the change in the vertical load on the tracks due to the weight shift, as in the understeering model, the front shows a higher lateral force, in the neutral steering model, both tracks show approximately the same lateral force and in the oversteering model, the rear track shows the highest overall lateral force.

We can observe that the magnitude of the lateral force changes between the linear and non-linear models, with a more realistic result in the non-linear model. These values can be directly attributed to the more realistic slip angles, as there is a direct correlation between these and the lateral force.

The yaw rate (Gillespie, 2021) can also be observed from these models; to do this, we calculate it for each model:

$$\omega = \vec{\omega} * \hat{Z} = \frac{V}{R} = \frac{V}{L/\tan(\alpha)}$$

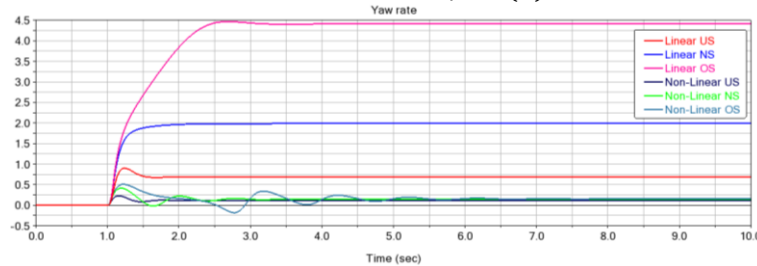


Figure 13. Bicycle models yaw rates

From the linear model, we can observe the expected underdamped, critically damped and overdamped response of the understeering, neutral-steering and oversteering models, respectively (Gillespie, 2021). Although this response is expected from linear models, this does not correspond to what happens in reality, as seen in the non-linear plots, since the linear model increases the lateral grip indefinitely.

From the non-linear model, we can observe the tyre skipping that happens on the oversteering model, while understeering and neutral-steering models displaying a similar reaction, but with exaggerated oscillations and settling time for the neutral-steering model. These results correlate well with the stable nature of understeering vehicles, the fast and precise response of neutral-steering vehicles and the instability of oversteering vehicles.

Maintaining a good balance between settling time and damping is needed in a vehicle to achieve both a quick reaction time and control predictability, it is for this reason that in motorsport-oriented vehicles, the tendency is closer to neutral-steer, as the driver is trusted to manage rough terrain and responsiveness is favoured (Blundell, 2004).

A plot of the position of the vehicle can also show us the difference in behaviour due to the change in maximum lateral grip:

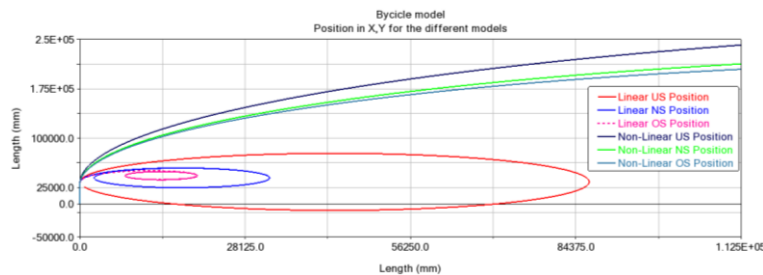


Figure 14. Bicycle models position along X,Y

When comparing the models, for both linear and non-linear, we observe that the oversteering model follows the tightest line, the neutral steering follows a medium line, and the understeering follows the widest line.

When contrasting the linear models with the non-linear models, we observe a clear difference in grip. The non-linear models are unable to converge to the trajectory of the linear models, as they more accurately represent the tyre behaviour, decreasing grip rather than increasing it at high slip angles.

Twin-track model

To evaluate the effects of vertical tyre load change during cornering and to represent a vehicle's steering system, a twin-track model was developed. This model consists of four wheels attached to a body, creating both the front and rear track of the vehicle. The rear track rotation is fixed to the rotation of the vehicle body, while the front track receives the steering input.

Model development

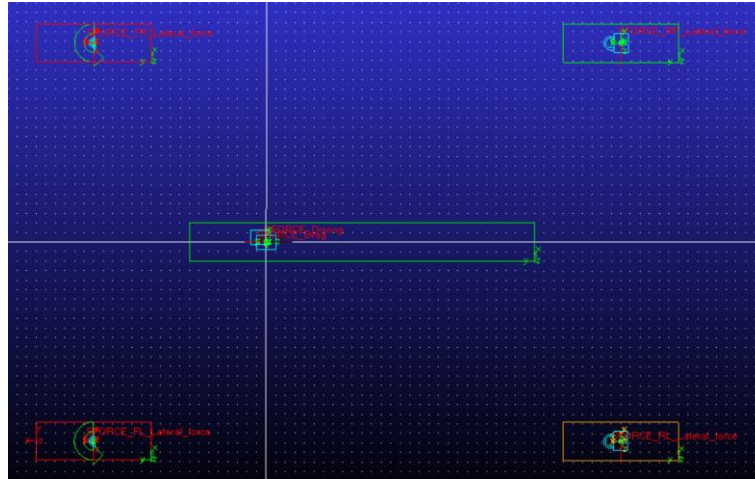


Figure 15. Twin-track model

For the twin-track model, Ackermann steering angle is considered (Balkwill, 2018):

$$\theta_{outer} = \theta + \arctan\left(\frac{L}{R \pm \frac{W}{2}}\right); \theta_{inner} = \theta + \arctan\left(\frac{L}{R \pm \frac{W}{2}}\right)$$

Lateral weight transfer between wheels for a steady-state turn is also considered (Milliken, 1995):

$$LLT \text{ (Lateral Load Transfer)} = accY * \frac{hCoG}{W}$$

Achieving a percentage value of the total load variation for the vehicle. This simpler formula is used as roll rates and tyre deflection rates for the vehicle are unknown. hCoG is assumed to be 0.5m for a roll motion (Hejtmánek, P., 2015).

Input parameters are available in table 3 on the appendix.

Results

Since the bicycle model confirmed the linear model to be unreliable, only the non-linear model was studied.

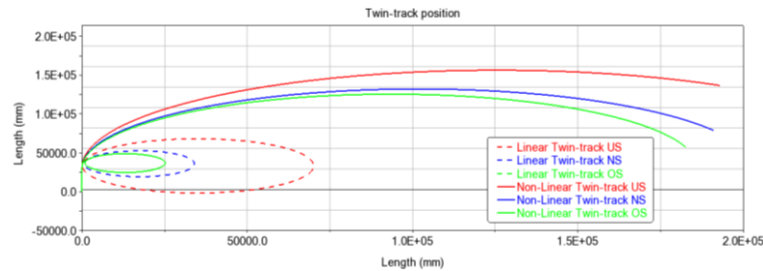


Figure 16. Twin-track X,Y position

From the position of the models, we can confirm the same behaviour as the bicycle models.

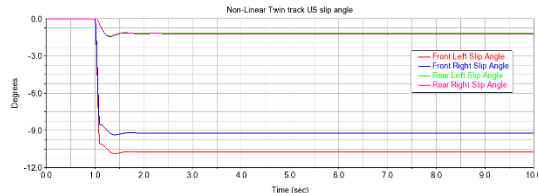


Figure 17. Twin-track US Slip angles

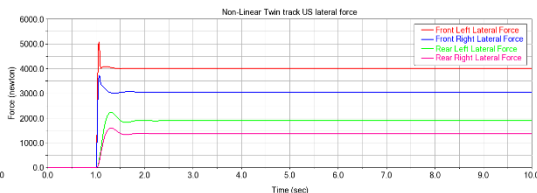


Figure 18. Twin-track US Lateral force

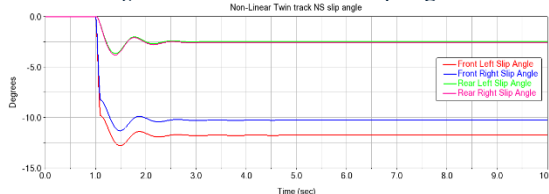


Figure 19. Twin-track NS Slip angles

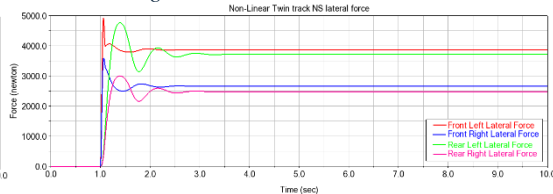


Figure 20. Twin-track NS Lateral force

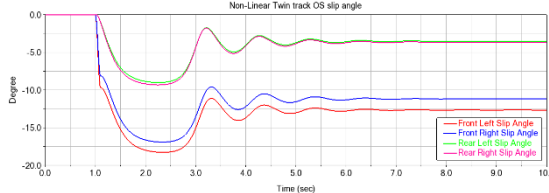


Figure 21. Twin-track OS Slip angles

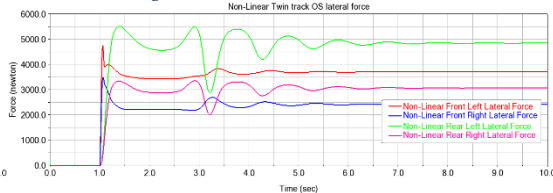


Figure 22. Twin-track OS Lateral forces

The slip angle plots reveal the effects of introducing Ackermann's steering. While the rear track is unaffected, the front track wheels show variations in slip, particularly noticeable in the understeer model, as more vertical load is placed on the track.

The lateral force plots demonstrate the effect of lateral and vertical load transfer on tyre force generation. We can observe not only a difference in generated force by wheels on the same track, but that this force varies depending on where the mass of the vehicle is located.

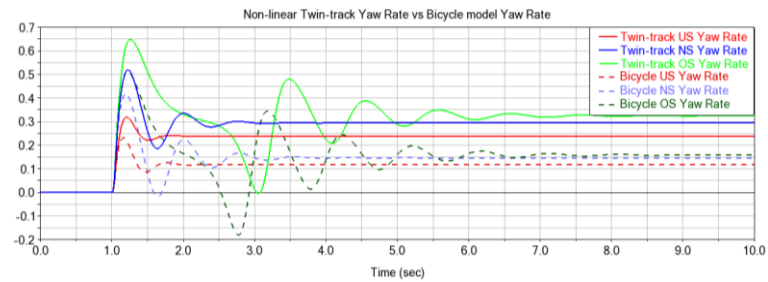
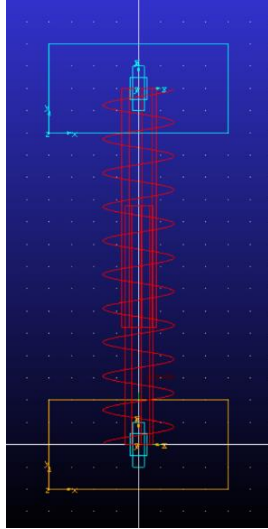


Figure 23. Twin-track model Yaw rates

The yaw rate for the non-linear twin-track models follows the same trends as for the bicycle model, confirming the correlation between the models. We can observe the effect of properly represented lateral load transfer, as the yaw magnitude for the twin-track is higher than for the bicycle model.

Suspension Dynamics and Ride Optimisation

Single-Degree of Freedom



To simulate suspension behaviour, firstly, a single element model is created, simulating the interaction between the sprung body and the road via a single suspension element, equivalent to the suspension elements present in the vehicle. This model allows to optimize the general tyre contact patch and uses the following reasonings (Balkwill, 2018):

$$\text{Equation of motion: } m\ddot{x} + c\dot{x} + kx = F_{road}(t)$$

$$\text{Damping ratio: } \zeta = \frac{C}{C_c} = \frac{C}{2\sqrt{k * m}} = 2 * m * \omega_n$$

$$\text{Natural frequency: } \omega_n = \sqrt{k/m}$$

Figure 24. SDoF model

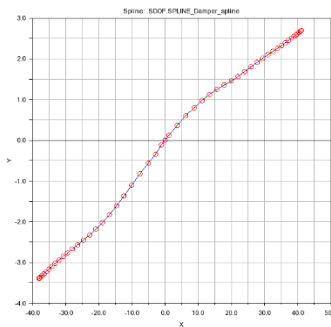


Figure 25. Damping spline

Input parameters are available in table 4 on the appendix.

The road force is inputted as a 4-post rig spline input, for a period of 59.9 seconds.

As this study treats a road racing vehicle, a high stiffness non-linear damping model is applied, in order to maximize the tyre contact patch on the road.

For later optimization of the model, damping coefficient and damping ratio design variables are included, a damper force measurement is also added.

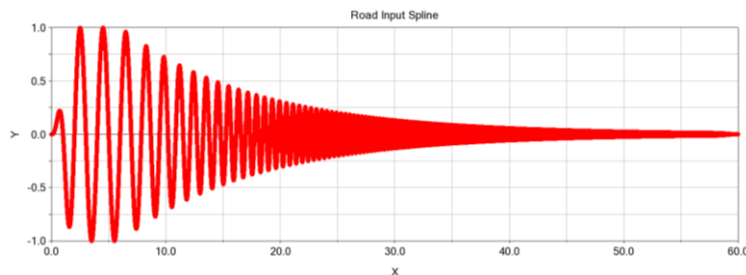


Figure 26. Road input spline

Optimization

We run a design optimization for the damping coefficient:

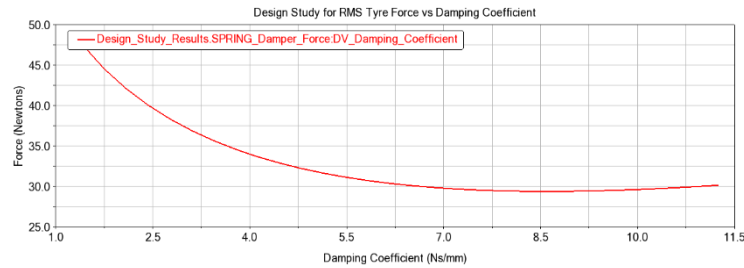


Figure 27. Spring force RMS damping coefficient optimization study

We achieve an optimal value for the damping coefficient of 8.5398 Ns/mm.

We then obtain the damping ratio and, by introducing it into the model, compare the results with the original and non-linear damping:

$$\text{Damping ratio: } \zeta = 0.277$$

This could be further optimized making use of models with more degrees of freedom, to achieve a more accurate representation of the vehicle.

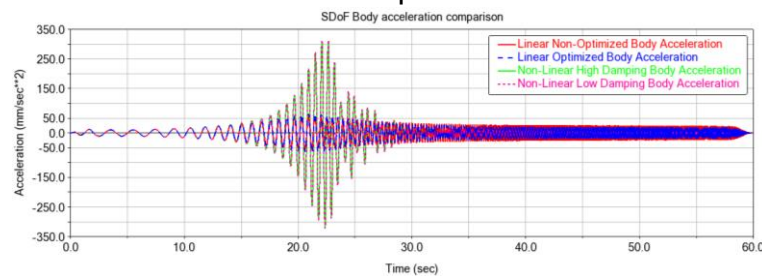


Figure 28. Comparison of vertical body acceleration for the SDoF model

A better response is achieved, improving tyre contact patch by the optimized damping, achieving more stable and consistent normal forces. Adding the non-linear damping for comparison, we can observe that the optimized value achieves a better overall result, as there is less amplitude of acceleration and a faster response.

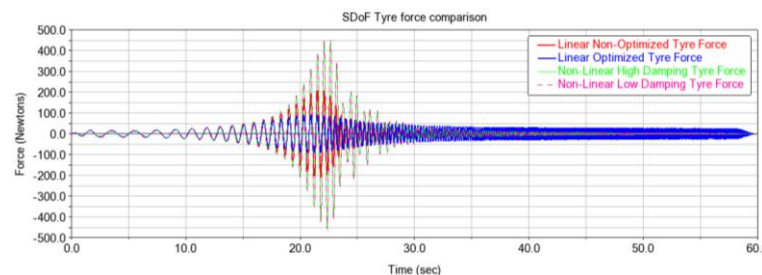
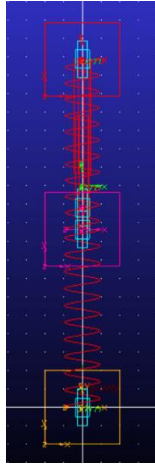


Figure 29. Comparison of tyre contact patch for the SDoF model

Comparing the effects of damping on the contact patch, we can observe a reduced overall amplitude for the optimized damping ratio. Adding the non-linear for comparison, the tyre contact patch gets improved for high frequency events.

These plots allow us to confirm the correct performance of the non-linear damper.

Two-Degree of Freedom



To create a TDoF model, an unsprung mass is added to the simulated bodies, this modifies the equations of motion (Balkwill, 2018):

$$\text{Sprung body equation of motion: } m_s \ddot{x}_s + c_s(\dot{x}_s - \dot{x}_u) + k_s(x_s - x_u) = F_{road}(t)$$

$$\text{Unsprung equation: } m_u \ddot{x}_u + c(\dot{x}_s - \dot{x}_u) + k_s(x_s - x_u) + k_u(x_u - x_s) = F_{road}(t)$$

Input road data is the same as shown in figure 20, the rest of the input parameters are available in table 6 on the appendix.

Figure 30. TDoF model

For later optimization, the variables mentioned in the SDoF model, tyre damping force, hub and vehicle displacements measurements are added.

Optimization

Optimization studies are run on the suspension's damping coefficient:

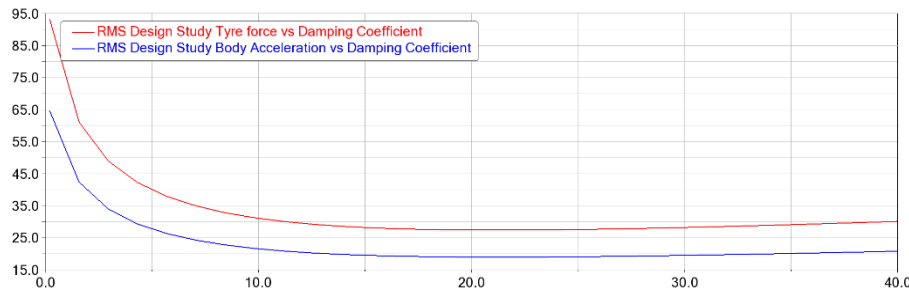


Figure 31. RMS Design studies for damping coefficient

On both studies, the optimal damping coefficient is 20.6872Ns/mm. We then obtain the optimal damping ratio:

$$\text{Damping ratio: } \zeta = 0.675$$

Introducing it into the model, we compare the optimised results with the original and non-linear damping.

When comparing the resonance between components, “The lower-frequency ride vibrations (0 - 25 Hz) are manifestations of dynamic behavior common to all rubber-tired motor vehicles” (Gillespie, 2021, p. 244). For this reason, we will concentrate on this frequency range for this and future studies.

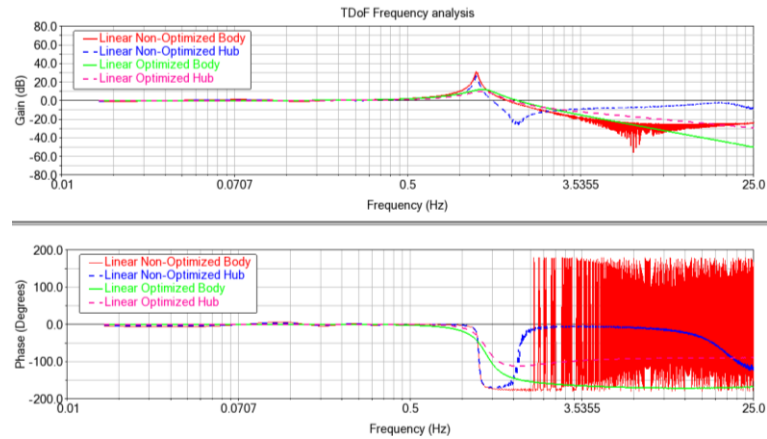


Figure 32. TDoF Component frequency study

Analysing the frequency of components, we can observe for both models the “body mode” (Balkwill, 2018) behaviour up until $\sim 0.85\text{Hz}$, where we enter “upright mode” and the bodies move counter-phase of each other. From the gain plot we can also observe a reduction in gain for the optimized model, leading to a lower amplitude of the oscillations and improved ride comfort and the tyre contact surface.

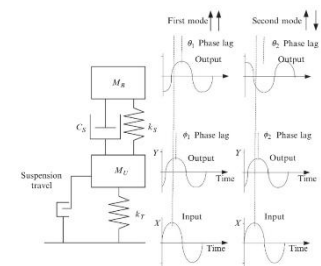


Figure 33. TDoF modes of vibration

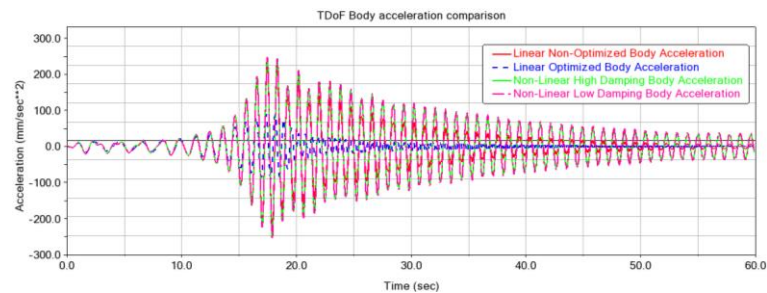


Figure 34. Comparison of TDoF model vertical body acceleration

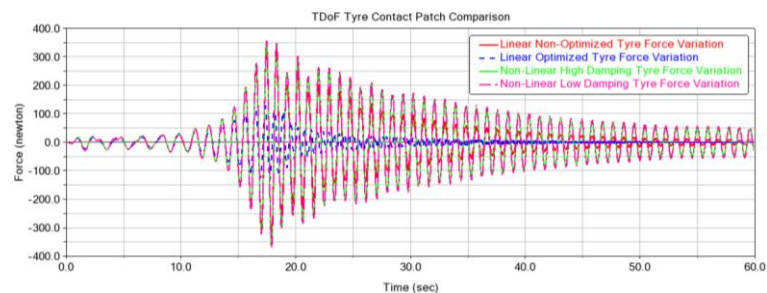


Figure 35. Comparison of TDoF model tyre force variation

Comparing the body’s vertical acceleration and tyre force, we can confirm the theories from analysing the frequencies. We can observe that the original metrics for the vehicle lack both in terms of tyre contact patch and ride quality, the non-linear damper reduces drastically the oscillations, sacrificing the tyre contact patch. In comparison, the optimized damper ratio maximizes the tyre contact patch while achieving a smaller body acceleration achieving the best result of the four configurations.

Faculty of Technology, Design & Environment
School of Engineering, Computing & Mathematics
Four-Degree of Freedom

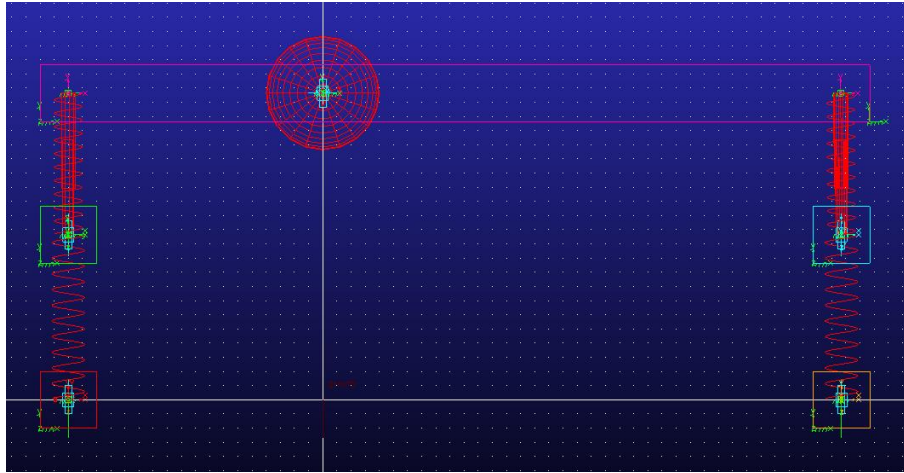


Figure 36. FDoF model

To account for the weight transfer during pitching and to include the track-specific stiffness and damping coefficient, a Four-Degree of Freedom model is created. To do this, a new CoG body is added alongside the sprung mass, allowing the measurement of pitch and acceleration, and a half-vehicle model is created to represent both front and rear tracks.

To implement the road input for a pitching moment experiment, we must include an offset between the front and rear track inputs:

$$\Delta t = \frac{L}{v} = \frac{2.735m}{30m/s} = 0.09117s$$

Measurements to identify front and rear hub displacements are placed. As the TDoF model demonstrated that the non-linear low damping suspension is the most inefficient, this suspension will not be compared on the FDoF model.

Input parameters are available in table 8 on the appendix.

Results

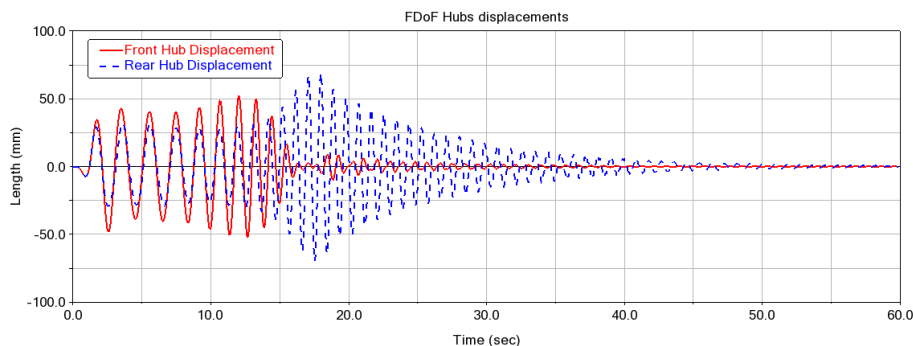


Figure 37. Original CoG location hub displacements

On this plot we can visualize the effects of weight transfer due to the position of the CoG, implying less vertical load present on the rear track as the CoG is positioned closer to the front track.

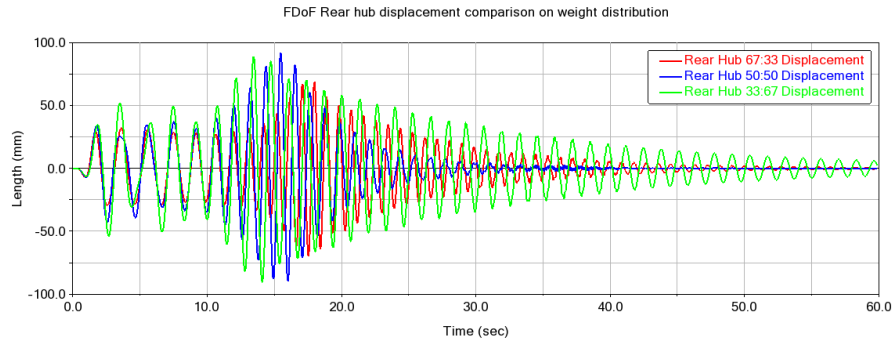


Figure 38. Rear hub displacement analysis

As we move the CoG rearwards, the displacement of the rear hub increases, as more vertical load is applied to the track, due to reduced energy dissipation capacity. This implies that, to reduce oscillations, softer springs are needed where more weight is present, usually the front track.

Optimization

Multiple optimization studies are run on the suspension's damping ratios to find the optimal value for the vehicle on a pitch movement:

Table 1. Optimization values for FDoF model

	Front Damping Ratio	Rear Damping Ratio
Body Vertical Acceleration	0.378850	0.434612
Body Pitch	0.942530	0.445748
Front Tyre Contact Patch	0.485678	0.448576
Rear Tyre Contact Patch	0.476250	0.402831
Average values	0.571	0.433

For OEM springs and tyres stiffness, the damping ratios that best optimise the vehicle's ride comfort and the tyres contact patches are 0.571 for the front and 0.433 for the rear.

Although these ratios imply an underdamped response, these do not imply a "soft" suspension, as typical damping ratio values for modern passenger vehicles stand between 0.2 and 0.4, meaning that this suspension setting can be considered as "hard", diminishing the ride quality.

This can be observed to be true, as the values achieved for the optimal vertical acceleration are 0.379 at the front and 0.436 at the rear, lower than the values used, creating a compromise for overall performance of the vehicle.

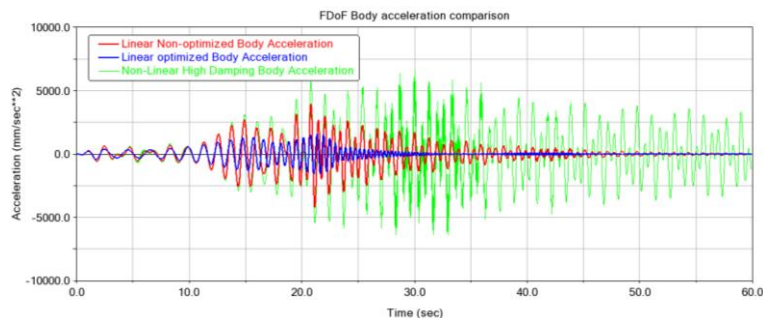


Figure 39. Comparison of vertical body acceleration for the FDoF model

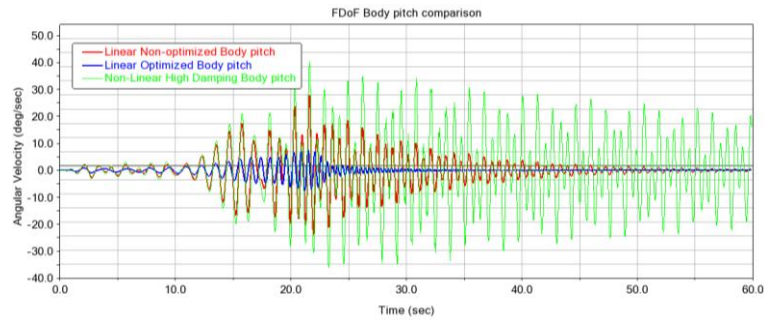


Figure 40. Comparison of body pitch for the FDoF model

Comparing the body's vertical acceleration and pitch, we can observe that the original suspension settings, although better than what's achieved by the non-linear settings, still lack on performance.

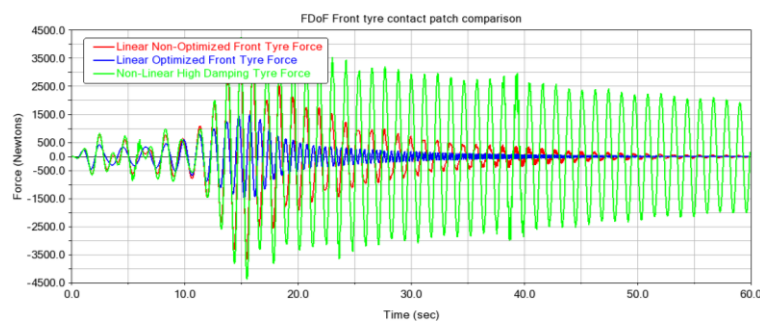


Figure 41. Comparison of front tyre force for the FDoF model

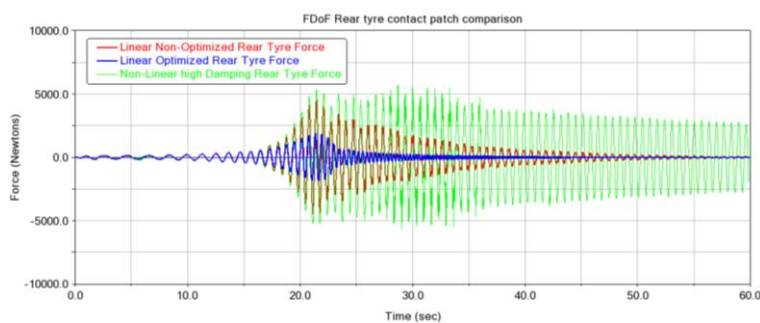


Figure 42. Comparison of rear tyre force for the FDoF model

Comparing the tyre forces achieved at both tracks, we can observe that the optimized suspension provides a faster damping, due to the higher damping ratio used, leading to less residual vibrations, maximizing tyre contact patch for both tracks. The non-linear suspension lack of performance for this model is noticeable as oscillations are maintained high during the whole experiment, achieving an unstable behaviour at both tracks.

Individual reflection

During the development of this portfolio, my understanding of the global implications of lateral and vertical forces on vehicle dynamics improved greatly, along with improving my knowledge of suspension dynamics and optimization by applying my theoretical knowledge to a practical model.

My knowledge of the ADAMS software was also expanded, since even though I had previous experience with the software, this work has allowed me to develop more complex models and to increase my ability to identify and solve problems arising in these models.

As additional work that would propose an improvement, I would have liked to include the development of a Seven-Degree of Freedom model, to perform a proper analysis of the vehicle suspension, as well as a MATLAB mathematical model for the bicycle and twin-track models, to validate the results via analytical formulations. I would have liked to have been able to analyse the frequency response of the FDoF model, as well as use a range of standard spring stiffnesses values for the suspension dynamics models and validate my findings with the results of a technical paper.

In conclusion, this portfolio has been a great work experience, as it has allowed me to develop and evaluate a range of vehicle models. The use of real vehicle parameters, such as the tyres cornering stiffnesses or the suspension characteristics, allowed me to further understand the real-world applications of these kinds of models when developing the characteristics of a vehicle, both for passenger and motorsports-oriented vehicles.

While characterising the vehicle's lateral load transfer and optimizing the vehicle's vertical acceleration and pitch was interesting to me, I found more interesting to see the implications of the suspension system in the overall vehicle's behaviour, as I had not considered the implications of suspension coupling and damping ratios prior to the making of this portfolio.

Bibliography

- Balkwill, J. (2018) *Performance Vehicle Dynamics*. Oxford: Elsevier.
- Gillespie, T.D. (2021) *Fundamentals of Vehicle Dynamics*. Warrendale: SAE International.
- Blundell, M. and Harty, D. (2004) *The Multibody Systems Approach to Vehicle Dynamics*: Elsevier.
- Milliken, W. F. and Milliken D. L. (1995) *Race Car Vehicle Dynamics*. Warrendale : SAE International.
- Lee, J.Y.S., Kim, S.H. and Lee, J.Y. (2017) 'Real-Time Autonomous Vehicle Control for High-Speed Maneuvers Using a Nonlinear Bicycle Model', *IEEE*. Available at: <http://dx.doi.org/10.1109/IVS.2017.7995816>
- Gvorotovic, M. (2013) 'Determination of Cornering Stiffness Through Integration of A Mathematical Model and Real Vehicle Exploitation Parameters', *FME Transactions*. Available at: https://www.mas.bg.ac.rs/_media/istrazivanje/fme/vol41/1/08_gvorotovic.pdf
- Honda Motor Company (2022) '2022 Honda Civic Type R specifications. Available at: https://www.automobile-catalog.com/car/2022/3121070/honda_civic_type_r.html#gsc.tab=0
- Perners, R. (2024) 'New approach to measure the vehicle centre of gravity height', *Perners Contacts*. Available at: <https://pernerscontacts.upce.cz/index.php/perner/article/view/701>
- Reddy, K. R. and Sujatha, C. (2001) 'Frequency Domain Sensitivity Analysis of Yaw Rate and Lateral Acceleration Response of Front Wheel Steering Vehicles', *SAE Technical Paper*. Available at: <https://doi-org.oxfordbrookes.idm.oclc.org/10.4271/2001-26-0035>
- Oraby, W. A. h., et al. (2007) 'Influence of Active Suspension Preview Control on the Vehicle Lateral Dynamics', *SAE Technical Paper*. Available at: <https://doi-org.oxfordbrookes.idm.oclc.org/10.4271/2007-01-2347>
- Ren, H., et al. (2014) 'Development of Effective Bicycle Model for Wide Ranges of Vehicle operations', *SAE Technical Paper*. Available at: <https://doi-org.oxfordbrookes.idm.oclc.org/10.4271/2014-01-0841>
- Balaga, S. R., Iaballa, M and Singh, K. B. (2024) 'Real-time cornering stiffness estimation and road friction state classification under normal driving conditions', *SAE Technical Paper*. Available at: <https://saemobilus.sae.org/papers/real-time-cornering-stiffness-estimation-road-friction-state-classification-normal-driving-conditions-2024-01-2650>
- Ding, Y. (2021) 'Simple understanding of the kinematic bicycle model', *Shuffleai*. Available at: https://www.shuffleai.blog/blog/Simple_Understanding_of_Kinematic_Bicycle_Model.html

Faculty of Technology, Design & Environment

School of Engineering, Computing & Mathematics

Unknown author (2023) '2023 Civic Si spring rates, motion ratio, and ride frequencies', *Civic XI Forum*. Available at:

<https://www.civicxi.com/forum/threads/2023-civic-si-spring-rates-motion-ratio-ride-frequencies-autocross.52362/>

SimpleTire (2024) 'Understanding Slip Angle & Differences in Tire Design'. Available at: <https://simpletire.com/learn/tire-news-information/slip-angle>

SuspensionSecrets (n.d.) 'Tyre Slip Angle'. Available at:

<https://suspensionsecrets.co.uk/tyre-slip-angle/#:~:text=Most%20racing%20tyres%20at%20the,a%2040%20degree%20slip%20angle>

Faculty of Technology, Design & Environment

School of Engineering, Computing & Mathematics

Appendix

Appendix 1. ADAMS bicycle model

Table 2. Input metrics for bicycle model

Vehicle metrics			Honda Civic FL5 Type-R Input metrics			Joints			
Name	Value	Unit	Coordinate system			Name	Type	Parts	Location
Vehicle body mass	1,430	kg	Front wheel centre	(0,900,0)	mm	Rear tyre to body	Fixed	Rear tyre; body	Rear tyre cm
Tyre mass	1	kg	Front wheel corner	(-100,600,0)	mm	Front tyre to body	Revolute	Front tyre; body	Front tyre cm
lxx	7.518E+05	kg.m ²	Body CoG Understeer	(0,0,0)	mm	Body to ground	Planar	Body; Ground	Body cm
lyy	1.127E+06	kg.m ²	Body CoG Neutral steer	(0,-467.5,0)	mm				
lzz	1.408E+06	kg.m ²	Body CoG Oversteer	(0,-562,0)	mm				
Wheelbase, L	2.735	m	Body corner	(-100,-1400,0)	mm				
CoG to front axle distance, a (assumed for a FF vehicle)	0.9	m	Rear wheel centre	(0,-1835,0)	mm				
Drag Coefficient	0.3		Rear wheel corner	(-100,-2135,0)	mm				
Forward velocity	30,000	mm/s							
Front Cornering Stiffness	1,500	N/deg							
Rear Cornering Stiffness	1,400	N/deg							

Appendix 2. ADAMS twin-track model

Table 3. Input metrics for twin-track model

Vehicle metrics			Honda Civic FL5 Type-R Input metrics			Joints			
Name	Value	Unit	Coordinate system			Name	Type	Parts	Location
Vehicle body mass	1,430	kg	Front wheel left centre	(-1041,900,0)	mm	FR tyre to body	Revolute	FR tyre; body	FR tyre cm
Tyre mass	1	kg	Front wheel right centre	(1041,900,0)	mm	FL tyre to body	Revolute	FL tyre; body	FL tyre cm
lxx	7.518E+05	kg.m ²	Front wheel left corner	(-1141,600,0)	mm	RR tyre to body	Fixed	RR tyre; body	RR tyre cm
lyy	1.127E+06	kg.m ²	Front wheel right corner	(1141,600,0)	mm	RL tyre to body	Fixed	RL tyre; body	RL tyre cm
lzz	1.408E+06	kg.m ²	Body CoG Understeer	(0,0,0)	mm	Body to ground	Planar	Body; Ground	Body cm
Wheelbase, L	2.735	m	Body CoG Neutral steer	(0,-467.5,0)	mm				
Width, W	2.082	m	Body CoG Oversteer	(0,-676,0)	mm				
CoG to front axle distance, a (assumed for a FF vehicle)	0.9	m	Body corner	(-1141,-1400,0)	mm				
Drag Coefficient	0.3		Rear wheel left centre	(-1041,-1835,0)	mm				
Forward velocity	30,000	mm/s	Rear wheel right centre	(1041,-1835,0)	mm				
Front Cornering Stiffness	1,500	N/deg	Rear wheel left corner	(-1141,-2135,0)	mm				
Rear Cornering Stiffness	1,400	N/deg	Rear wheel right corner	(-1141,-2135,0)	mm				

Motions		
Name	Value	Units
Outer steering angle	10.88	deg
Inner steering angle	9.29	deg

Appendix 3. ADAMS SDoF model

Table 4. Input metrics for SDoF model

Vehicle metrics			Honda Civic FL5 SDoF Input metrics		
Name	Value	Unit	Coordinate system		
Vehicle body mass	1430	kg	Name	Value	Unit
lxx	7.518E+05	kg.m ²	Road centre	(0,0,0)	mm
lyy	1.127E+06	kg.m ²	Body centre	(0,562,0)	mm
lzz	1.408E+06	kg.m ²			
Suspension height	482	mm			
Spring stiffness	165.814	N/mm			
Spring stiffness deviation	(4, 400)	N/mm			
Damping coefficient	2.462				
Damping coefficient deviation	(1, 20)				

Joints			
Name	Type	Parts	Location
Road to ground	Translational	Road; ground	Road cm
Body to road	Translational	Body; road	Body cm

Table 5. Optimization values for SDoF model

SDoF Optimized Values		
Name	Value	Unit
Damping coefficient	8.5398	Ns/mm
Critical Damping	30.7970	Ns/mm
Natural frequency	10.7682	rad/s
Damping ratio	0.2773	

Appendix 4. ADAMS TDoF model

Table 6. Input metrics for TDoF model

Honda Civic FL5 TDoF Input metrics					
Vehicle metrics			Coordinate system		
Name	Value	Unit	Name	Value	Unit
Vehicle body mass	1430	kg	Road centre	(0,0,0)	mm
lxx	7.518E+05	kg.m ²	Upright centre	(0,582,0)	mm
lyy	1.127E+06	kg.m ²	Body centre	(0,1082,0)	mm
lzz	1.408E+06	kg.m ²			
Upright mass	90	kg	Joints		
lxx	4.161E+02	kg.m ²	Name	Type	Parts
lyy	4.161E+02	kg.m ²			Location
lzz	4.161E+02	kg.m ²	Road to ground	Translational	Road; ground
Suspension height	482	mm			Road cm
Body height	1082	mm	Body to ground	Translational	Body; ground
Standard spring stiffness (car total)	165.814	N/mm			Body cm
Spring stiffness deviation	(2, 400)	N/mm	Upright to ground	Translational	Upright; ground
Standard damping coefficient	0.8				Upright cm
Damping coefficient deviation	(0.2, 20)				
Standard tyre stiffness (car total)	113.928	N/mm			
Tyre stiffness deviation	(4, 200)	N/mm			

Table 7. Optimization values for TDoF model

TDoF Optimized Values		
Name	Value	Unit
Damping coefficient	20.7862	Ns/mm
Critical Damping	30.7970	Ns/mm
Natural frequency	10.768	rad/s
Damping ratio	0.675	

Appendix 5. ADAMS FDoF model

Table 8. Input metrics for FDoF model

Honda Civic FL5 FDoF Input metrics					
Vehicle metrics			Coordinate system		
Name	Value	Unit	Name	Value	Unit
Vehicle body mass	1340	kg	Road front centre	(-900,0,0)	mm
Body lxx	7.518E+05	kg.m ²	Upright front centre	(-900,582,0)	mm
Body lyy	1.127E+06	kg.m ²	Road rear centre	(1835,0,0)	mm
Body lzz	1.408E+06	kg.m ²	Upright rear centre	(1835,582,0)	mm
Upright mass	45	kg	Body original CoG	(0,1082,0)	mm
Upright lxx	4.161E+02	kg.m ²	Body 50:50 distribution CoG	(467.5,1082,0)	mm
Upright lyy	4.161E+02	kg.m ²	Body 33:67 distribution CoG	(935,1082,0)	mm
Upright lzz	4.161E+02	kg.m ²			
Suspension height	482	mm			
Joints					
Name	Type	Parts	Location		
Front road to ground	Translational	Front road; ground	Front road cm		
Rear road to ground	Translational	Rear road; ground	Rear road cm		
CoG to ground	Translational	Body; ground	CoG cm		
Front Upright to ground	Translational	Front Upright; ground	Front Upright cm		
Rear Upright to ground	Translational	Rear Upright; ground	Rear Upright cm		
Body pitch	Revolute	CoG; Body	CoG cm		

Table 9. Optimization values for FDoF model

FDoF Optimized Values		
Name	Value	Unit
Front Damping ratio	0.571	
Rear Damping ratio	0.433	
Front Critical Damping	17.0136	Ns/mm
Rear Critical Damping	24.4806	Ns/mm
Front Natural frequency	6.3484	rad/s
Rear Natural frequency	9.1346	rad/s